Multi-scale random walk models for reactive transport processes in fracture-matrix systems

Delphine Roubinet, Philippe Gouze, Alexandre Puyguiraud, Marco Dentz

Multi-scale random walk models for reactive transport processes in fracture-matrix systems

Delphine Roubinet[a,c], Philippe Gouze[a], Alexandre Puyguiraud[b], Marco Dentz[b],

[a] *Geosciences Montpellier, University of Montpellier, CNRS, Montpellier, France*
[b] *Spanish National Research Council (IDAEA-CSIC), Barcelona, Spain*
[c] *Corresponding author: delphine.roubinet@umontpellier.fr*

Abstract

Random walk methods are particularly well suited for modeling (anomalous) transport processes in complex systems, from heterogeneous porous domains to fractured rocks. Taking full advantge of their multi-scale attributes, these methods can be integrated into multi-scale modeling strategies where they are used for (i) performing small-scale simulations with a high level of description of the heterogeneities, (ii) defining statistical functions that describe these heterogeneities at a larger scale, and (iii) providing upscaled descriptions of the processes while taking into account the impact of the small-scale heterogeneities. In this work, we define such a strategy considering (i) structural heterogeneities with heterogeneous porosity fields incorporated into fracture-matrix systems and (ii) the reactivity of the system with chemical reactions that are not restricted to linear first-order reactions as it is the case in existing upscaled formulations. To this end, we develop two new modeling methods: the Reactive-Time Domain Random Walk (R-TDRW) and Upscaled Reactive TDRW (UR-TDRW) approaches at small and large scale, respectively. The numerical methods and multi-scale strategy are presented with

a general formulation and applied to single-species transport and reaction in fracture-matrix systems. We analyze the impact of different levels of structural heterogeneities, and the impact of the reactivity, on the breakthrough curves computed at both scales and on the statistical functions that are used in the multi-scale strategy. This strategy is validated by demonstrating the good agreement between the results obtained at different scales, showing promising applications for future work in large-scale fracture networks.
Keywords: Random walk methods, Heterogeneous systems, Fracture-matrix systems, Chemical reactions, Statistical description, Upscaling methods

1. Introduction

Modeling reactive transport processes that occur in the natural environment is a key challenge for numerous research fields and applications. It requires to couple flow, transport and chemical processes that are characterized by different space and time scales [e.g., 1, & references therein] [e.g., 2]. Considering advective and diffusive mechanisms in heterogeneous geological formations amplifies the ranges of the considered scales and leads to the development of new modeling approaches and the adaptation of existing ones [e.g., 3, 4, 5, 6].

Random walk (RW) or particle-based methods are well suited to model and upscale anomalous hydrodynamic transport behavior for various scales, processes and degrees of heterogeneities [e.g., 5, 1, 7, 8, 9]. Taking into account the impact of small-scale properties in large-scale simulations can be done by parameterizing upscaled RW methods such as Continuous Time

Random Walk (CTRW) with spatial and temporal statistics of the particle displacement at the small scale. When these statistics are defined from numerical simulations, they allow to capture the impact of heterogeneous properties on mass transfer at various scales and to represent for example pre-asymptotic behavior that cannot be described by standard upscaling methods relying on the existence of a Representative Elementary Volume (REV) [10, 11, 12]. RW methods are also able to deal with a large range of transport regimes including large values of the Peclet number, in particular when they are used in dual-porosity, mobile-immobile and fracture-matrix systems [13, 14, 15]. In these cases, analytical formulations that are often called memory functions, are used to parametrize the diffusion times in the low porosity domain. This results in running large-scale transport simulations with reasonable computational resources while taking into account heterogeneous properties of the advection-dominant domain, while standard methods (such as finite volume, finite difference or finite element) require a costly increase in discretization to avoid numerical dispersion issues.

These features and successful applications in simulating transport processes in heterogeneous systems make RW methods an ideal candidate to establish efficient and robust reactive transport models in heterogeneous systems. First efforts into this challenge led so far to models that are used in academic research, but they have a strong potential for a larger audience. However, the RW transport models that are adapted to dual-porosity/mobile-immobile/fracture-matrix systems mentioned before, are based on analytical solutions restricting the simulations to homogeneous properties of the low porosity domain, linear relationship between the mobile and immobile do-

main concentrations and linear first-order chemical reactions [e.g., 16, 13]. Analytical formulations of the impact of chemical reactions on the fate of particles are also used in mesh-free (homogeneous) domains by expressing the survival probability of each particle [e.g., 17, 18, 19, 20]. As a result, performing efficient simulations of reactive transport processes that are adapted to structural heterogeneities and various kinds of chemical reactions, requires the development of new modeling approaches and strategies.

In this work, we present a modeling approach that allows simulating advective and diffusive processes with structural heterogeneities that range from heterogeneous matrix porosity fields to the fracture/matrix contrast, and chemical reactions that are not restricted to linear first-order expressions. To this end, we take advantage of the multi-scale attributes of the TDRW approach and its ability to simulate advective and diffusive mechanisms in heterogeneous systems and we extend its formulation to reactive transport problems in the frame of a multi-scale modeling strategy. This is inspired by the work of Gouze et al. [12] for inert solute in heterogeneous porous domains, and it is done here through the development of two numerical methods. (i) The R-TDRW (Reactive-TDRW) approach that solves the reactive transport (2-dimensional) problem at the scale of description of the domain properties (i.e., the pixels that represent void and solid or Darcy-scale properties such as porosity). (ii) The UR-TDRW (Upscaled Reactive-TDRW) approach that solves the problem on an 1-dimentional upscaled description of the system, corresponding to a mobile-immobile (or dual-porosity) representation of the domain that is parameterized by small-scale simulations. In both methods, solute transport is represented by the displacement of particles

while the chemical reactions are modeled at the pixel scale in the small-scale simulations assuming no changes in porosity during the simulations.

General formulations of the R-TDRW and UR-TDRW methods for multi-species and reactions are presented in Section 2 and the considered multi-scale strategy in Section 3. Applications to fracture-matrix systems with a single species transport and reaction are shown in Section 4, where the presented numerical methods and strategy are validated with analytical solutions. Section 5 is dedicated to analyzing the impact of structural, hydraulic and chemical properties on transport behavior and the ability of both R-TDRW and UR-TDRW models to describe it.

2. Methodological background

2.1. Problem formulation

Consider the transport of N_s reactive species such that the solute concentration $c_s(\mathbf{x}, t)$ of species s ($s = 1, ..., N_s$) at position $\mathbf{x}$ and time t satisfies the reactive transport equation

$$\frac{\partial[\phi(\mathbf{x})c_s(\mathbf{x},t)]}{\partial t} + \nabla \cdot [\mathbf{u}(\mathbf{x})c_s(\mathbf{x},t)] = \nabla \cdot [\mathbf{D}(\mathbf{x})\nabla c_s(\mathbf{x},t)] - r_s(c_s, \mathbf{x}, t) \quad (1)$$

with ϕ the porosity, $\mathbf{u}$ the flow velocity, $\mathbf{D}$ the diffusion tensor matrix and r_s the reaction term related to species s.

In mobile-immobile systems, ϕ is set to 1 in the mobile domain and $\mathbf{u}$ to 0 in the immobile domain. Considering isotropic domain properties, the tensor $\mathbf{D}$ is defined as the effective diffusion coefficient $D_e = D_m\phi^n$ with D_m the molecular diffusion coefficient and $n \geq 1$ the porosity exponent that denotes the effect of tortuosity for $n > 1$ [21] and with $D_e = D_m$ in the

mobile domain. Different reaction terms r_s can be considered in the mobile and immobile domains with the expressions $r_{s,m}$ and $r_{s,im}$, respectively.

2.2. Small-scale modeling approach

Small-scale simulations are performed on two-dimensional domains that are discretized into pixels of regular size Δx. Equation (1) is solved in these systems by using a reactive TDRW approach as outlined below.

The displacement of particles is modeled with the TDRW approach, which has been formulated for diffusive processes [22] and advective and diffusive processes [11] in heterogeneous and homogeneous porosity fields, respectively. It is expressed here for advective and diffusive processes with space-dependent porosity properties using the recursive relationships (or Random Walk process)

$$\mathbf{x}_i(n+1) = \mathbf{x}_j(n) + \xi_{ij}, \quad t(n+1) = t(n) + \theta_j, \tag{2}$$

which express the displacement from pixel j to pixel i of a particle being at pixel j after n jumps with the transition length $|\xi_{ij}|$ and transition time θ_j. The probability w_{ij} of jumping from pixel j to one of its neighboring pixels i is defined as

$$w_{ij} = \frac{b_{ij}}{\sum_{k\in\mathcal{V}_j} b_{kj}} \quad \text{with} \quad b_{ij} = D_{ij}\Delta x + u_{ij}\Delta x^2 H(u_{ij}). \tag{3}$$

In expression (3), $\mathcal{V}_j$ is the set of neighboring pixels of pixel j, the function $H(u_{ij})$ is set to 1 if $u_{ij} > 0$ and 0 otherwise, u_{ij} is the flow velocity from pixel j to i and D_{ij} is the harmonic mean of the diffusion coefficients in pixles i and j. The time θ_j associated with the jump from pixel j to one of

its neighboring pixels is drawn from the exponential distribution $\psi(t, \tau_j)$ of mean τ_j that is expressed as

$$\psi(t, \tau_j) = \frac{\exp(-t/\tau_j)}{\tau_j} \quad \text{with} \quad \tau_j = \frac{\phi_j V_j}{\sum_{k \in \mathcal{V}_j} b_{kj}} \tag{4}$$

with ϕ_j and V_j the porosity and volume of pixel j.

Reactions are modeled at the pixel scale with the concentration $c_{j,s}$ of solute species s in pixel j that is defined as

$$c_{j,s} = \sum_{k \in \mathcal{K}_j} m_{k,s}/(\phi_j V_j), \tag{5}$$

where $\mathcal{K}_j$ is the set of particles that are present in pixel j and $m_{k,s}$ the mass of solute species s carried by particle k. Using an operator splitting approach, concentration and particle mass in the pixel are updated isochronically, that is at discrete times $t_n = n\Delta t$ ($n = 1, 2, \dots$) according to the chemical reaction rate $r_s(c_s, \mathbf{x}, t)$ associated with the solute species s. This implies that

$$c'_{j,s} = c_{j,s} + \Delta t \frac{r_s}{\phi_j}, \quad m'_{k,s} = c'_{j,s} \phi_j \frac{V_j}{N(\mathcal{K}_j)}, \quad k \in \mathcal{K}_j \tag{6}$$

with $N(\mathcal{K}_j)$ the number of particles in the set $\mathcal{K}_j$. Note that after the reaction step, mass is distributed equally between all particles according to the new concentration. Thus, before the reaction step, particles may carry different masses, while after the reaction step, they are homogenized.

2.3. Upscaled models

The upscaled formulation of the R-TDRW approach presented in Section 2.2 relies on a 1D representation of the mobile domain over which advective and diffusive processes are considered and coupled to diffusion in the

(not physically represented) immobile domain. The governing equations are derived from expressions (2) and (3), which leads to moving the particles along the 1D mobile domain according to the recursive relation

$$\mathbf{x}_i(n+1) = \mathbf{x}_j(n) + \xi_{ij} \tag{7}$$

with the large-scale spatial transition ξ_{ij}, and the downstream (W_d) and upstream (W_u) probabilities

$$W_d = \frac{D_m}{2D_m + U\Delta x}, \quad W_u = \frac{D_m + U\Delta x}{2D_m + U\Delta x}, \tag{8}$$

where D_m, U and Δx are the molecular diffusion coefficient, upscaled flow velocity and pixel size of the 1D mobile domain, respectively.

The displacement expression (7) is associated with the recursive time relation

$$T(n+1) = T(n) + \theta_j, \quad \theta_j = T_j^m + T_j^{im}, \quad T_j^m \sim \psi(t, \tau_j), \tag{9}$$

where θ_j represents the time of the particle jump from pixel j to one of its neighboring pixels, including the times T_j^m and T_j^{im} spent in the mobile and immobile domains, respectively. T_j^m is defined from the 1D-reduced form of the TDRW approach, corresponding to the exponential distribution $\psi(t, \tau_j)$ given in (4) for which the distribution mean reduces to $\tau_j = \Delta x^2/(2D_m + U\Delta x)$. Conversely, T_j^{im} is an upscaled description of the diffusive process in the immobile domain, whose distribution $P_{\tau_{im}}$ is derived from analytical solutions or small-scale numerical models.

The displacement and time recursive expressions (7) and (9) are associated with the survival probability $\mathcal{S}_j^s$, which is the probability that a particle keeps carrying species s after jumping from pixel j to one of its neighboring

pixels. $\mathcal{S}_j^s$ is an upscaled description of the reactivity of the system that depends on the time spent in the mobile and immobile domains and is also derived from analytical solutions or small-scale numerical simulations.

3. Multi-scale modeling strategy

3.1. Upscaled parameter definition

The upscaled model presented in Section 2.3 requires to define the time spent in the immobile domain T_j^{im} and the survival probability $\mathcal{S}_j^s$ that are associated with the particle jump from pixel j to one of its neighboring pixels and the species s carried by the particle. These variables are expressed as

$$T_j^{im} = \mathcal{H}(N_j^e) \sum_{e=1}^{N_j^e} \tau_{j,e}^{im}, \quad \mathcal{S}_j^s = \mathcal{S}_{j,m}^s \prod_{e=1}^{N_j^e} \mathcal{S}_{j,im}^s, \tag{10a}$$

with

$$\mathcal{H}(N_j^e) = \begin{cases} 0, & \text{if } N_j^e = 0, \\ 1, & \text{otherwise,} \end{cases} \qquad N_j^e \sim P_p(k, \lambda_j), \quad \tau_{j,e}^{im} \sim P_{\tau_{im}}, \tag{10b}$$

$$\mathcal{S}_{j,d}^s(\tau) = \frac{1}{N_p} \sum_{k \in \mathcal{S}_\tau} w_{k,d}^s / w_{k,d}^{s,0}, \quad d = m, im. \tag{10c}$$

In expressions (10), we consider the following definitions.

N_j^e is the number of transfers from the mobile to immobile domains. As done in [12], this number is drawn from the Poisson distribution $P_p(n, \lambda_j) = \lambda_j^n e^{-\lambda_j}/n!$ where n is the number of events and λ_j is the distribution parameter defined as $\lambda_j = T_j^m \gamma$ with γ the time rate for the number of considered events. The macro-scale parameter γ is defined from small-scale simulations as $\gamma = 1/\langle \tau_m \rangle_p$, τ_m being the local mobile time (i.e., the time spent in the

mobile domain between two transfer events, called survival time in [12]) and $\langle . \rangle_p$ the average value over the particles.

The upscaled immobile time T_j^{im} depends on the immobile local time $\boldsymbol{\tau}_{j,e}^{im}$, which is the time spent in the immobile domain during the e^{th} transfer event (i.e., the time required to go back to the mobile domain for the e^{th} transfer event) and is drawn from the immobile local time distribution $P_{\tau_{im}}$.

$\mathcal{S}_{j,m}^s$ and $\mathcal{S}_{j,im}^s$ are the survival probabilities associated with the mobile time T_j^m and local immobile times $\boldsymbol{\tau}_{j,e}^{im}$, respectively, that are defined from small-scale simulations. In expression (10c), $\mathcal{S}_\tau$ is the set of particles that spent time τ in the considered domain and enter and exit the domain with the weight $w_{k,d}^{s,0}$ and $w_{k,d}^s$ in species s, respectively. In the same expression, N_p is the total number of particles considered in the simulation.

3.2. Upscaled parameter computation

The upscaled parameter γ, distribution $P_{\tau_{im}}$ and probabilities $\mathcal{S}_{j,m}^s$ and $\mathcal{S}_{j,im}^s$ previously defined are computed from small-scale simulations that are performed with the R-TDRW approach presented in Section 2.2. Whereas these variables could be evaluated from full small-scale simulations in which the initial domain is fully represented with both the mobile and immobile zones, the number of required simulations and their complexity are minimized here by adapting the small-scale configurations as explained below.

As described in Table 1, computing the time rate of mobile-immobile transfers γ requires to represent both the mobile and immobile domains (*Full configuration*), the distribution of immobile local times $P_{\tau_{im}}$ and the survival probability in the immobile domain $\mathcal{S}_{j,im}^s$ can be evaluated from configurations that only represent the immobile zone (*Immobile configuration*), and

the survival probability in the mobile domain $\mathcal{S}^s_{j,m}$ from configurations that only represent the mobile zone (*Mobile configuration*). In terms of micro-scale parameter values, γ and $P_{\tau_{im}}$ characterize the structural properties of the system independently of the reactivity of the system, implying that they can be evaluated for inert solutes with $r_{s,d} = 0$ ($d = im, m$), whereas $\mathcal{S}^s_{j,m}$ and $\mathcal{S}^s_{j,im}$ characterize the reactivity of the system in the mobile and immobile domain, respectively, independently of the physical and structural properties of the immobile and mobile domain, respectively.

Upscaled properties	Domain configuration	Small-scale properties
γ	*Full configuration*	$\mathbf{u}$, ϕ, $r_{s,im} = 0$, $r_{s,m} = 0$
$P_{\tau_{im}}$	*Immobile configuration*	ϕ, $r_{s,im} = 0$
$\mathcal{S}^s_{j,m}$	*Mobile configuration*	u, $r_{s,m}$
$\mathcal{S}^s_{j,im}$	*Immobile configuration*	ϕ, $r_{s,im}$

Table 1: Domain configurations and parameter values considered to define the upscaled properties γ, $P_{\tau_{im}}$, $\mathcal{S}^s_{j,m}$ and $\mathcal{S}^s_{j,im}$.

4. Configurations and validation

4.1. Considered configurations and parameters

Consider the fracture-matrix system shown in Figure 1 that corresponds to advection and diffusion processes in a fracture coupled with pure diffusion in the surrounding matrix and chemical reaction in both domains. Applying

the modeling approaches and strategy presented in Sections 2 and 3 results in a full 2D description of the system at the small scale with R-TDRW and an upscaled 1D description at the fracture scale with UR-TDRW, in which the surrounding matrix is taken into account without being physically representated. This system is considered with the two sets of parameters *Param1* and *Param2* that are provided in Table 2. *Param1* corresponds to cases studied in Tang et al. [23] and *Param2* to parameter values mentionned in Dentz et al. [13] and Gouze et al. [12].

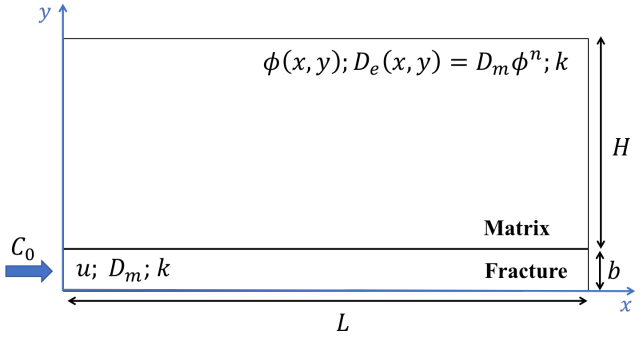

Figure 1: Fracture-matrix configuration with fracture length and aperture L and b, respectively, fracture flow velocity u, molecular diffusion coefficient D_m, matrix domain width H, matrix porosity and diffusion coefficient fields $\phi(x,y)$ and $D_e(x,y)$, respectively, porosity exponent n, reaction rate coefficient k and concentration of injected solute on the left side of the fracture C_0.

The impact of the matrix structural heterogeneities is studied by comparing the results obtained with (i) homogeneous porosity fields where the porosity $\phi(x,y)$ is set to a constant value ϕ_0 and (ii) heterogeneous porosity fields defined from multi-gaussian distributions whose averaged value is set to ϕ_0. Various heterogeneous fields are simulated by defining a threshold porosity value ϕ_{th} below which ϕ is set to 0, resulting in increasing the

Parameters	*Param1*	*Param2*
L [m]	0.05 ; 0.1	0.1
b [m]	10^{-4}	10^{-4}
u [m/s]	1.1574×10^{-7} ; 1.1574×10^{-6}	10^{-7};10^{-6};10^{-5}
D_m [m^2/s]	1.6×10^{-10}	10^{-9}
H [m]	1.0	0.1
ϕ [-]	0.01	0.1
ϕ_{th} [-]	-	0.0;0.1;0.15
n [-]	1	2
k [s^{-1}]	0.0 ; 1.7797×10^{-9}	0.0;10^{-9};10^{-8};10^{-7};10^{-6}

Table 2: Parameter values associated with the fracture-matrix configuration shown in Figure 1. ϕ is the porosity value when considering homogeneous porosity fields and the average value for heterogeneous porosity field with ϕ_{th} the porosity threshold (Figure 2).

heterogeneity field when increasing parameter ϕ_{th}. Figure 2 illustrates such heterogeneous porosity fields described with the harmonic, geometric and arithmetic averages equal to 0.01. This field is generated with 1,000 pixels in each direction. However, when a larger number of pixels is necessary, we extend its size by duplicating the porosity field in the required direction(s).

The numerical simulations are performed by setting the size of each mesh element to 5×10^{-5} m for both R-TDRW and UR-TDRW. The number of particles and time steps used ranges from 10^4 to 10^8 and from 10 to 10^5, respectively, depending on the considered configurations. Injection of

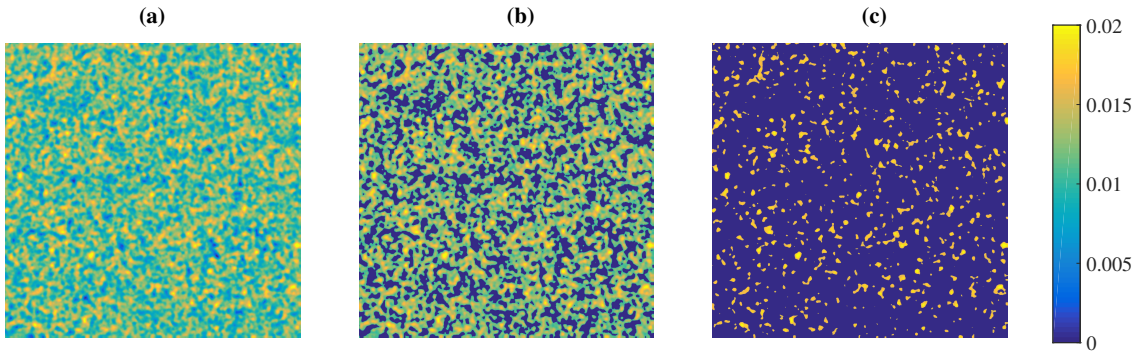

Figure 2: Heterogeneous porosity fields from multi-gaussian distribution with ϕ_{th} set to (a) 0.0, (b) 0.01 and (c) 0.015. Color scale denotes porosity.

solute at the inlet of the fracture is simulated by inserting particles in the corresponding pixel at the beginning of the simulations. The concentration at the oulet is evaluated by recording the particle arrival times in the fracture pixel located at $x = L$.

4.2. Validation of the numerical methods

The numerical methods and upscaling strategy are validated with the analytical solution provided by Tang et al. [23] for a continuous injection in a single fracture surrounded with an infinite matrix. Assuming no diffusion in the fracture (i.e., $D_m = 0$ m^2/s in the fracture), the solute concentration at position x along the fracture relatively to the injected concentration is

expressed as

$$C_f(x,t) = \frac{e^{-kx/u}}{2}\left[e^{-\sqrt{k}x/(uA)}\mathrm{erfc}\left(\frac{x}{2uAT} - \sqrt{k}T\right)\right.$$
$$\left. + e^{\sqrt{k}x/(uA)}\mathrm{erfc}\left(\frac{x}{2uAT} + \sqrt{k}T\right)\right], \tag{11}$$
$$A = \frac{b}{2\phi\sqrt{D_0}}, \quad T = \mathcal{H}(t - x/u)\sqrt{t - x/u},$$

where k is the decay constant of the chemical reaction $r = kc$.

Figure 3a shows the good agreement between analytical solution (11) and the numerical methods R-TDRW and UR-TDRW for the set of parameters *Param1*, thus providing a first validation of both the numerical methods and upscaling strategy. For $L = 0.1$ m (thick black and blue curves in Figure 3a), these parameters come from the reactive transport problems studied in Tang et al. [23] with $u = u_1 = 1.1574 \times 10^{-6}$ m/s and $u = u_2 = 1.1574 \times 10^{-7}$ m/s, denoted as "high and low-velocity" cases in Tang et al. [23], and $k = k_1 = 0$ and $k = k_2 = 1.7797 \times 10^{-9}$ s^{-1}, corresponding to inert and reactive transport. The parameters used to run the R-TDRW simulations are provided in Table 2, while those required for UR-TDRW simulations are given in Table 3 with the upscaled parameter γ computed from the R-TDRW simulations as explained in Section 3. The probability density function (pdf) of local immobile times $P_{\tau_{im}}$ and the survival probability S, computed from R-TDRW simulations and also required for UR-TDRW simulations (see Section 3), are provided in Figure 3b and c (black curves), respectively. The results presented in Figure 3a for $L = 0.1$ m show that the considered chemical reaction does not impact the relative concentration observed at the fracture outlet for the high-velocity case ($u = u_1$), since the curves overlap for $k = k_1$ (no reaction) and $k = k_2$ (corresponding to half life of $t_{1/2} = 12.35$ years). In

this case, the solute exits the system through the fracture outlet before experiencing a decrease in concentration due to the radioactive decay. On the contrary, applying the decay constant k_2 for the low-velocity case ($u = u_2$) results in decreasing the solute concentration of late arrival times in comparison with the inert case ($k = k_1$), for which the relative concentration C_f reaches 1 for long times. Results without reaction for a smaller value of L are also plotted to show the impact of this parameter on the transport behavior (thin red and green curves in Figure 3a). It results in the same curve shapes for which the concentrations are observed at earlier times and upscaled with the same upscaled parameters and functions.

L [m]	0.05 ; 0.1
u [m/s]	1.1574×10^{-7} ; 1.1574×10^{-6}
D_m [m^2/s]	0.0
γ [s^{-1}]	0.0013

Table 3: Parameter values that are used in the UR-TDRW simulations for the inital set of parameters *Param1* given in Table 2. L, u and D_m correspond to the fracture parameters defined in Figure 1 and γ to the upscaled parameter described in Section 3 and obtained for a homogeneous matrix.

The R-TDRW method and upscaled methodology are also validated by comparing the upscaled functions $P_{\tau_{im}}$ and S, determined from R-TDRW and used in UR-TDRW, with analytical solutions. In Figure 3b, the black solid line corresponds to $P_{\tau_{im}}$ computed with R-TDRW and the magenta thick solid line to the analytical solution presented in Appendix A. The differences observed between these two curves for short times is explained

by the numerical approximations that are made below the pixel size and the similar behavior of the curves after these short times validates the numerical method.

The additional curves shown in Figure 3b are presented for comparing the impact of the matrix heterogeneities on the distribution of local immobile times $P_{\tau_{im}}$. We observe that $P_{\tau_{im}}$ is similar when considering a homogeneous porosity field with $\phi = 0.01$ and a heterogeneous porosity field with average porosity set to 0.01 and no porosity threshold (black curve). $P_{\tau_{im}}$ is modified when applying a porosity threshold equal and larger than 0.01 (from dashed blue to dotted green). Increasing the porosity threshold ϕ_{th} from 0.01 to 0.017 results in decreasing the proportion of large values of $P_{\tau_{im}}$ showing that the matrix heterogeneity prevents the particles from spending long times in the matrix. In other words, increasing the threshold value acts as decreasing the effective depth of the matrix.

Finally, in Figure 3c, the solid lines represent the analytical solution

$$S(t) = \exp(-kt), \tag{12}$$

which denotes the relative concentration $c(t)/C_0$ when considering the reaction $\mathrm{d}c/\mathrm{d}t = -kc$ with the initial concentration C_0. We see that this solution overlaps with the survival probability computed with the R-TDRW method (crosses) for various values of the half-time $t_{1/2}$.

5. Results and analysis

In this section we aim at evaluating how the structural, physical and chemical properties impact the transport of reactive elements in fracture-matrix systems. To do so, we consider the set of parameters *Param2* in

Table 2 and compute the corresponding breakthrough curves (BTCs) with R-TDRW and UR-TDRW for various Péclet numbers, porosity fields and chemical reactions (Figure 4). The upscaled functions and parameters, which are computed with the R-TDRW simulations and used for the UR-TDRW simulations, are shown in Figure 5 and Tables 4 and 5, and the computational performances of both methods are discussed in Section 5.4.

ϕ [-]	0.1	0.11	0.113085	0.12
γ [s^{-1}]	0.00801581	0.00966572	0.0102022	0.0114561

Table 4: Values of the upscaled parameter γ for homogeneous porosity fields.

ϕ_{th} [-]	0.0	0.1	0.15	0.2
γ [s^{-1}]	0.0109525	0.00933908	0.00248995	0.0

Table 5: Values of the upscaled parameter γ for heterogeneous porosity fields with the arithmetic, harmonic and geometric porosity means equal to 0.113085, 0.105057 and 0.109444, respectively.

5.1. Hydraulic properties

Figure 4a shows the BTCs for various values of the Péclet number that is defined as $Pe = ub/D_0$ with u, b and D_0 the configuration parameters described in Figure 1. As expected, we observe that decreasing the Péclet number (i.e., decreasing the contrast between the advective and diffusive properties) results in changing the shape of the BTCs. It goes from an asymmetric curve with a large quantity of particles arriving at early times due to advection and a slope of -3/2 showing late arrival times due to diffusion

($Pe = 1$, solid black curve), to a symmetric curve characteristic of purely diffusive process ($Pe = 10^{-2}$, dash-dotted red curve). For $Pe = 1$ and $Pe = 10^{-1}$, the slope is modified at time $\bar{t}_H = 5 \times 10^7$ s (vertical thin dashed black line), which corresponds to the averaged time required to reach the matrix wall (i.e., the time required to cover the matrix width distance H), showing the impact of the finite matrix block size on the arrival times.

Figure 4a also shows how the upscaled modeling approach UR-TDRW can be used to reproduce the results obtained with the small-scale simulations. This is done by using the pdf of local immobile times defined for a homogeneous matrix from the R-TDRW method (black curve in Figure 5a) and setting the upscaled parameter γ to 0.008 (Table 4). The results provided by UR-TDRW fit well that from R-TDRW, except for the early times of $Pe = 10^{-2}$, which shows the limitation of representing a (almost) purely diffusive behavior (i.e., small Péclet numbers) with a mobile-immobile (or fracture-matrix) upscaled representation.

5.2. Structural heterogeneities

Considering the hydraulic properties associated with $Pe = 1$, Figure 4b shows the impact of the matrix heterogeneities on the BTCs considering multi-Gaussian distributions for the heterogeneous porosity fields (Figure 2). Changing the matrix porosity field from homogeneous (with $\phi = 0.1$, black curve) to heterogeneous (with $\phi_{th} = 0.0$, dashed blue curve) does not impact the particle arrival times since the curves overlap. However, increasing the parameter ϕ_{th} from 0.0 (dashed blue curve) to 0.1 (dash-dotted red curve) results in increasing the proportion of early arrival times and thus decreasing the quantity of particles that arrive at late times. This phenomenon is

enhanced when we keep increasing ϕ_{th} from 0.1 to 0.15 (from dashed red to dash-dotted green curves) where we observe in addition an earlier peak of arrival times. This is observed until ϕ_{th} reaches the value 0.2 above which no changes are observed and the curve is similar to the case $\phi = 0.0$ (solid magenta curve), i.e., it behaves as if there is no matix. These results show that increasing the porosity threshold results in decreasing the mass transfer from fracture to matrix until that there is no mass transfer (when $\phi_{th} \geq 0.2$), corresponding to a pure fracture configuration (without surrounding matrix). Note also that, for $\phi_{th} \geq 0.1$, particles exit the matrix before they reach the matrix wall, since the distribution of trapping times is cut off before the characteristic time $\bar{t}_H$ as shown in Figure 4a.

For all these cases, we see that the UR-TDRW method fits well the small-scale simulations. These results are obtained with the pdfs of local immobile times shown in Figure 5a. From this figure, we observe that adding heterogeneities in the porosity field does not impact the distribution $P_{\tau_{im}}$ since the curves for a homogeneous (solid black curve) and heterogeneous matrix without threshold (dashed blue curve) overlap. Increasing the porosity field complexity (by increasing ϕ_{th} from dashed blue to dotted green curves) leads to a decrease in the late arrival times and slightly increases the porportion of short arrival times, showing that it is harder for the particles to circulate deep into the matrix.

In addition to the distributions $P_{\tau_{im}}$ displayed in Figure 5a, the values of the upscaled parameter γ shown in Tables 4 and 5 are used to obtain the UR-TDRW results shown in Figure 4b. From Table 4, we see that when ϕ increases from 0.1 to 0.12 (for homogeneous porosity fields), γ increases from

0.008 to 0.011, leading to more transfer from the fracture to the surrounding matrix. Note that these values of ϕ correspond to the various averaged values (arithmetic, harmonic and geometric) of the multi-Gaussian porosity field considered in the heterogeneous case with $\phi_{th} = 0.0$. However, these changes in γ are too small to impact the particle arrival times since they lead to the same UR-TDRW BTCs (black and blue crosses in Figure 4b). When considering heterogeneous porosity fields with ϕ_{th} ranging from 0.0 to 0.2, γ varies from 0.01 (which is equivalent to the homogeneous case with the porosity set to the arithmetic mean) to 0.0 (Table 5). This shows that (i) the value of γ associated with the heterogeneous case with no threshold ($\gamma = 0.01$ for $\phi_{th} = 0.0$) is similar to that of γ associated with the homogeneous porosity set to the arithmetic mean of the multi-Gaussian field ($\gamma = 0.01$ for $\phi = 0.11$) and (ii) γ decreases from 0.01 to 0.0 when ϕ_{th} increases from 0.0 to 0.2, showing that increasing the matrix heterogeneities reduces the fracture-matrix transfers. This is observed until the extreme case $\phi_{th} = 0.2$ for which there is no fracture-matrix transfer and the system behaves as a single fracture with no surrounding matrix. Here we focused on the impact of structural heterogeneity of the matrix on the trapping rate. Note however, that varying the fracture aperture b also impacts on the trapping rate. [9] show for a homogeneous fracture-matrix system that the trapping rate is inversely proportional to the fracture aperture.

5.3. Chemical reactions

We consider now that the transported solute is subject to the chemical reaction described by the reaction term r. For simplicity, we assume that the same reaction occurs in the fracture and matrix but different reactions could

be modeled if needed. To focus on the impact of the chemical properties, the simulations are run with the homogeneous porosity field described before and, as in the previous cases, the Péclet number is set to 1. Figures 4c and d show the BTCs computed with TDRW and UR-TDRW for the linear reaction $r = kc$ and the non-linear reaction $r = kc^2$, respectively. The survival probabilities that are computed from TDRW and used in UR-TDRW are shown in Figures 5b-c, and the upscaled parameter γ is set to the value obtained for a homogeneous porosity field with $\phi = 0.1$, i.e., $\gamma = 0.008$.

Figure 4c shows the BTCs for various values of the Damkhöler number Da defined as $Da = k/(D_m LH)$. From these results, we observe that (i) similar values are obtained for $0 \leq Da \leq 10^{-2}$ (solid black curve) implying that in these cases the reaction rate coefficient k is too small to impact the particle arrival times whose behavior is defined by the transport properties, and (ii) when $Da \geq 10^{-1}$ the chemical reaction impacts the particle arrival times with a decrease of the proportion of long arrival times when increasing Da. In the latter cases, the mass transported by the particles that remain a long time in the system is consumed by the chemical reaction, whereas no impact is observed on the short arrival times. The same behavior is osberved for the non-linear reaction (Figure 4d) with a less important impact of the reaction on the arrival times due to the inital mass transported by the particles that is smaller than 1.

Figure 4c-d also shows that the results provided by R-TDRW and UR-TDRW overlap, which demonstrates the ability of the UR-TDRW method to reproduce linear and non-linear reactions considered at the small scale. The behavior of the survival probabilities $\mathcal{S}$ (Figures 5b-c) is consistent with the

observations made on the BTCs with (i) no impact of the chemical reaction for $0 \leq Da \leq 10^{-2}$ with $\mathcal{S} = 1$ (i.e., 100% of the particles survive), (ii) a decrease of the survival probability (i.e., an increase of the mass consumed by the reaction), when $Da \geq 10^{-1}$ increases, and (iii) larger values of $\mathcal{S}$ when considering the non-linear reaction (i.e., less mass consummed by the reaction) because the initial transported mass is smaller than 1.

5.4. Computational performances

The computational performances of the TDRW and UR-TDRW methods are analyzed in the sense of the computational time required to perform the simulations. In order to evaluate the impact of the Peclet and Damkhöler numbers on these performances, we report in Table 6 the computational times required to obtain the results presented in Figures 4a and c. All the TDRW and UR-TDRW simulations are run with 10^6 and 10^5 particules, respectively, except when the Peclet number is set to 10^{-1} and 10^{-2} for TDRW and $Pe = 10^{-2}$ for UR-TDRW for which N_p and N_P are set to 10^5 and 10^4, respectively. These changes in the number of particles are necessary to maintain reasonable computation times when decreasing the Peclet number. When doing so, high computation times are observed because it leads to configurations where there is more exchange between the fracture and surrounding matrix, i.e. more particles transfer from the fracture to the matrix. These additional transfers result in additional operations that increase the computation times for both TDRW and UR-TDRW, to which is added the time spent by diffusion in the matrix for TDRW. This is illustrated by (i) similar computation times when decreasing the number of particles of one order of magnitude while decreasing Pe from 1 to 10^{-1} for TDRW and

from 10^{-1} to 10^{-2} for UR-TDRW, and (ii) an increase of one order of magnitude of the computation time when decreasing Pe from 10^{-1} to 10^{-2} with the same number of particles for TDRW.

On the contrary, we observe that working on a large range of the Damkhöler number does not impact the computation time and the required number of particles since increasing the reactivity of the system does not require additional operations in the implemented methods.

Finally, comparing the computation times of the TDRW and UR-TDRW methods for all the simulations considered in Table 6, shows that the upscaling method results in reducing the computational times from one to two orders of magnitude.

		$Da = 0$			$Da = 0 - 10$
		$Pe = 1$	$Pe = 10^{-1}$	$Pe = 10^{-2}$	$Pe = 1$
TDRW	N_p [-]	10^6	10^5	10^5	10^6
	t_s [s]	1.4×10^4	1.5×10^4	1.2×10^5	$[1.4 \times 10^4 : 1.5 \times 10^4]$
UR-TDRW	N_P [-]	10^5	10^5	10^4	10^5
	T_s [s]	118	965	854	[118 : 129]

Table 6: Computational performances for the results presented in Figure 4a ($Da = 0$ and $Pe = 1, 10^{-1}, 10^{-2}$) and Figure 4c ($Da = 0 - 10$ and $Pe = 1$) with N_p and t_s the number of particles and CPU time, respectively, associated with the TDRW method, and N_P and T_s their counterparts for the UR-TDRW method.

6. Conclusions and discussion

The multi-scale modeling strategy presented in this work enables us to provide upscaled simulations of transport processes in fracture-matrix systems. This is done by taking into account (i) the contrast in transport properties between fracture and matrix (advection in the fracture and diffusion in the matrix), (ii) the structural heterogeneities at the matrix scale with heterogeneous porosity fields and (iii) the reactivity of the system with linear and non-linear reactions. Defining statistical functions that describe the structural heterogeneities on one side, and the reactivity of the system on the other side, enables us to decouple these two features that have a determinant impact on the breakthrough curves. The good agreement between the results obtained at different scales shows the validity of the multi-scale procedure, which could be used in future work for large-scale fractured rocks simulations with multi-species transport and reactions.

Our study also shows the good computational performance offered by the upscaling method compared to the small-scale modeling approach. In addition, this performance can be easily grealty improved by using parallel computing since the changes in transport and reactivity of each particle are independent. For the small-scale models, the interest of parallel computing needs to be evaluated because it requires to stop the particles at each chemical time step in order to gather the information needed to simulate the chemical reaction. This analysis will need to be done to conduct more complex small-scale simulations such as 3D heterogeneous problems, which will require additional computing resources. Reducing the computational cost of more complex configurations could also be done by using hybrid models that

combine different scales and kinds of solutions [e.g., 24, 25, 26].

For modeling specific realistic multi-species chemical systems, a chemical reaction rate parameter $r_s = f(C_j, C_j^*, S, ...)$ can be defined for each of the N_s species and parametrized by the species concentration $C_j(\mathbf{x}, t)$ (with $j = 1, ..., N_s$), some chemical constants denoting for instance the equilibrium concentration or the concentration required for nucleation C_j^* and any other time-dependant and, or, space dependent parameters such as the reactive surface area $S(\mathbf{x}, t)$. The impact of the reactions on the structural properties of the system can also be considered by taking into account the changes in matrix porosity and fracture aperture (and for instance the induced changes in the reactive surface area) due to precipitation and dissolution reactions. The structural properties will be assumed constant over a chemical time step during which particles are moved, and they will be updated at the end of each time step when the chemical reactions are considered.

The upscaling approach embraced in this paper uses a statistical characterization of the small scale transport and reaction processes in order to establish the upscaled reactive transport model. While details on the exact small scale behaviors are not retained, as in general in upscaling or coarse-graining efforts, the proposed approach retains statistical information on the fluctuations of small scale processes, which are encoded in the distribution of residence times in the matrix, the representation of trapping as a Poisson process, and the survival probabilities that account for chemical reaction. The parameters of the upscaled model reflect the small scale physical processes, namely advective-diffusive transport (U and D_m) and reaction (survival probability $\mathcal{S}_m^s$) in the fracture, and mass transfer between fracture and matrix

(trapping rate γ), and retention (immobile time distribution $P_{\tau_{im}}$) and reaction ($\mathcal{S}^s_{im}$) in the matrix. The number of parameters remains the same when increasing the complexity of the system by introducing a distribution of porosities in the matrix. However, if complexity is added by introducing additional physical processes, additional parameters need to be included to represent these additional processes in the large scale. The numerical simulations of the detailed small scale processes are an important step in the upscaling effort, because it enables to gain a physical understanding of the small scale processes and their impact on the large scale behavior, which enables the systematic derivation of a physically sound large scale model.

Acknowledgement

The authors gratefully acknowledge the support of the CNRS-PICS project CROSSCALE (Project No. 280090).

Appendix A. Analytical solution for $P_{\tau_{im}}$

The distribution of trapping times inside the matrix is obtained from the solution of a first passage or, strictly speaking, a first return problem. The distribution of trapping times is given by the distribution of times that particles spend in the matrix after they enter the matrix at the fracture matrix interface. This is a well-known problem, and it is also well-known that there is a conceptual problem regarding the return problem, which is solved by considerding diffusion on a grid and place the particle initially at a distance ϵ from the interface. Thus, we solve now the first-passage problem from a point close to the interface across the interface. This means, we

consider the diffusion problem

$$\frac{\partial c(y,t)}{\partial t} - D\frac{\partial^2 c(y,t)}{\partial y^2} = 0, \tag{A.1}$$

where D is the diffusion coefficient in the immobile region. We consider an instantaneous point injection at $y = y'$ and a zero flux boundary at $y = H$. This problem can be solve straightforwardly in Laplace space. The Laplace transform of (A.1) reads as

$$\lambda c*(y,\lambda) - D\frac{\partial^2 c^*(y,\lambda)}{\partial y^2} = \delta(y - y'), \tag{A.2}$$

The solution for $c^*(y,\lambda)$ is

$$c^*_+(y,\lambda) = \cosh\left[(y-H)\right]\sinh\left(y'\sqrt{\frac{\lambda}{D}}\right)B \tag{A.3}$$

for $y > y'$ and

$$c^*_-(y,\lambda) = \cosh\left[(y'-H)\right]\sinh\left(y\sqrt{\frac{\lambda}{D}}\right)B, \tag{A.4}$$

for $y < y'$. We used that concentration is continuous at $y = y'$. The Dirac Delta on the right side of (A.2) implies a jump condition for the flux. This means that

$$\int_{y'-\epsilon}^{y'+\epsilon} dy\left[\lambda c^*(y,\lambda) - D\frac{\partial^2 c^*(y,\lambda)}{\partial y^2}\right] = 1. \tag{A.5}$$

Due to continuity of $c^*(y,\lambda)$ at $y = y'$, this equation implies that

$$\frac{\partial c^*_-(y,\lambda)}{\partial y} - \frac{\partial c^*_+(y,\lambda)}{\partial y} = \frac{1}{D}. \tag{A.6}$$

Thus, we obtain for B

$$B = \frac{1}{\sqrt{\lambda D}\cosh(L\sqrt{\lambda/D})}. \tag{A.7}$$

Thus, the solution for $c^*(y,\lambda)$ is

$$c = \begin{cases} \frac{\cosh[(y-H)]\sinh\left(y'\sqrt{\frac{\lambda}{D}}\right)}{\sqrt{\lambda D}\cosh(H\sqrt{\lambda/D})} & y > y' \\ \frac{\cosh[(y'-H)]\sinh\left(y\sqrt{\frac{\lambda}{D}}\right)}{\sqrt{\lambda D}\cosh(H\sqrt{\lambda/D})} & y < y'. \end{cases} \tag{A.8}$$

The first passage time distribution is given by the solute flux through the boundary at $y = 0$, this means

$$\psi^*(\lambda|y') = D\frac{\partial c_-^*(y,\lambda)}{\partial y}\bigg|_{y=0}. \tag{A.9}$$

Thus, we obtain the explicit Laplace space expression

$$\psi^*(\lambda|y') = \frac{\cosh\left[(1-\frac{y'}{H})\sqrt{\lambda\tau_D}\right]}{\cosh(\sqrt{\lambda\tau_D})}, \tag{A.10}$$

where we defined $\tau_D = H^2/D$. In the limit $H \to \infty$, we obtain the Levy distribution

$$\psi^*(\lambda|y') = \exp\left(-y'\sqrt{\frac{\lambda}{D}}\right), \tag{A.11}$$

This expression can be Laplace inverted in closed form, which gives the Levy-Smirnov density

$$\psi(t) = \frac{y\exp(-y^2/4Dt)}{\sqrt{4Dt^3}} \tag{A.12}$$

The memory function is defined in terms of the trapping time distribution as

$$\varphi^*(\lambda) = \lim_{y'\to 0}\frac{1}{\lambda\langle\tau\rangle}\left[1-\psi^*(\lambda)\right]. \tag{A.13}$$

The mean trapping time is obtained from (A.10) as

$$\langle\tau\rangle = -\frac{\partial\psi^*(\lambda|y')}{\partial\lambda}\bigg|_{\lambda=0}. \tag{A.14}$$

Thus, we obtain

$$\langle \tau \rangle = \frac{y'}{H} \tau_D. \tag{A.15}$$

Inserting (A.10) and (A.15) gives

$$\varphi^*(\lambda) = \frac{1}{\sqrt{\lambda \tau_D}} \tanh\left(\sqrt{\lambda \tau_D}\right), \tag{A.16}$$

References

[1] B. Berkowitz, I. Dror, S. K. Hansen, H. Scher, Measurements and models of reactive transport in geological media, Reviews of Geophysics 54 (2016) 930–986. doi:10.1002/2016RG000524.

[2] J.-M. Etancelin, P. Moonen, P. Poncet, Improvement of remeshed lagrangian methods for the simulation of dissolution processes at pore-scale, Advances in Water Resources 146 (2020) 103780. doi:10.1016/j.advwatres.2020.103780.

[3] B. Berkowitz, Characterizing flow and transport in fractured geological media: A review, Advances in Water Resources 25 (2002) 861–884. doi:10.1016/S0309-1708(02)00042-8.

[4] S. Neuman, Trends, prospects and challenges in quantifying flow and transport through fractured rocks, Hydrogeology Journal 13 (2005) 124–147. doi:10.1007/s10040-004-0397-2.

[5] S. Painter, V. Cvetkovic, J. Mancillas, O. Pensado, Time domain particle tracking methods for simulating transport with retention and first-order transformation, Water Resources Research 44 (2008). doi:10.1029/2007WR005944, w01406.

[6] T. Aquino, T. Le Borgne, The chemical continuous time random walk framework for upscaling transport limitations in fluid–solid reactions, Advances in Water Resources 154 (2021) 103981. doi:10.1016/j.advwatres.2021.103981.

[7] B. Noetinger, D. Roubinet, A. Russian, T. Le Borgne, F. Delay, M. Dentz, J.-R. de Dreuzy, P. Gouze, Random walk methods for modeling hydrodynamic transport in porous and fractured media from pore to reservoir scale, Transport in Porous Media (2016) 1–41. doi:10.1007/s11242-016-0693-z.

[8] P. Gouze, A. Puyguiraud, D. Roubinet, M. Dentz, Pore-scale transport in rocks of different complexity modeled by random walk methods, Transport in Porous Media (2021). doi:10.1007/s11242-021-01675-2.

[9] J. D. Hyman, M. Dentz, Transport upscaling under flow heterogeneity and matrix-diffusion in three-dimensional discrete fracture networks, Adv. Water Resour. 155 (2021) 103994. doi:https://doi.org/10.1016/j.advwatres.2021.103994.

[10] F. Gjetvaj, A. Russian, P. Gouze, M. Dentz, Dual control of flow field heterogeneity and immobile porosity on non-fickian transport in berea sandstone, Water Resources Research 51 (2015) 8273–8293. doi:10.1002/2015WR017645.

[11] A. Russian, M. Dentz, P. Gouze, Time domain random walks for hydrodynamic transport in heterogeneous media, Water Resources Research 52 (2016) 3309–3323. doi:10.1002/2015WR018511.

[12] P. Gouze, A. Puyguiraud, D. Roubinet, M. Dentz, Characterization and upscaling of hydrodynamic transport in heterogeneous dual porosity media, Advances in Water Resources 146 (2020). doi:10.1016/j.advwatres.2020.103781.

[13] M. Dentz, P. Gouze, J. Carrera, Effective non-local reaction kinetics for transport in physically and chemically heterogeneous media, Journal of contaminant hydrology 120-21 (2011). doi:10.1016/j.jconhyd.2010.06.002.

[14] V. R. Gisladottir, D. Roubinet, D. M. Tartakovsky, Particle methods for heat transfer in fractured media, Transport in Porous Media (2016) 1–16. doi:10.1007/s11242-016-0755-2.

[15] V. Cvetkovic, Statistical Formulation of Generalized Tracer Retention in Fractured Rock, Water Resources Research 53 (2017) 8736–8759. doi:10.1002/2017WR021187.

[16] P. C. Lichtner, Q. Kang, Upscaling pore-scale reactive transport equations using a multiscale continuum formulation, Water Resources Research 43 (2007). doi:10.1029/2006wr005664.

[17] D. A. Benson, M. M. Meerschaert, Simulation of chemical reaction via particle tracking: Diffusion-limited versus thermodynamic rate-limited regimes, Water Resources Research 44 (2008).

[18] D. Ding, D. A. Benson, A. Paster, D. Bolster, Modeling bimolecular reactions and transport in porous media via particle tracking, Advances in Water Resources 53 (2013) 56–65. doi:10.1016/j.advwatres.2012.11.001.

[19] D. Bolster, A. Paster, D. A. Benson, A particle number conserving l agrangian method for mixing-driven reactive transport, Water Resources Research 52 (2016) 1518–1527. doi:10.1002/2015wr018310.

[20] L. J. Perez, J. J. Hidalgo, M. Dentz, Reactive random walk particle tracking and its equivalence with the advection-diffusion-reaction equation, Water Resources Research 55 (2019) 847–855. doi:10.1029/2018WR023560.

[21] P. Gouze, Y. Melean, T. Le Borgne, M. Dentz, J. Carrera, Non-fickian dispersion in porous media explained by heterogeneous microscale matrix diffusion, Water Resources Research 44 (2008). doi:10.1029/2007WR006690.

[22] M. Dentz, P. Gouze, A. Russian, J. Dweik, F. Delay, Diffusion and trapping in heterogeneous media: An inhomogeneous continuous time random walk approach, Advances in Water Resources 49 (2012). doi:10.1016/j.advwatres.2012.07.015.

[23] D. H. Tang, E. O. Frind, E. A. Sudicky, Contaminant transport in fractured porous media: Analytical solution for a single fracture, Water Resources Research 17 (1981) 555–564. doi:10.1029/WR017i003p00555.

[24] A. M. Tartakovsky, D. M. Tartakovsky, T. D. Scheibe, P. Meakin, Hybrid simulations of reaction-diffusion systems in porous media, Siam Journal on Scientific Computing 30 (2008). Doi:10.1137/070691097.

[25] I. Battiato, D. M. Tartakovsky, A. M. Tartakovsky, T. Scheibe, Hybrid models of reactive transport in porous and fractured

media, Advances in Water Resources 34 (2011) 1140–1150. doi:10.1016/j.advwatres.2011.01.012.

[26] D. Roubinet, D. M. Tartakovsky, Hybrid modeling of heterogeneous geochemical reactions in fractured porous media, Water Resources Research 49 (2013) 7945–7956. doi:10.1002/2013WR013999.

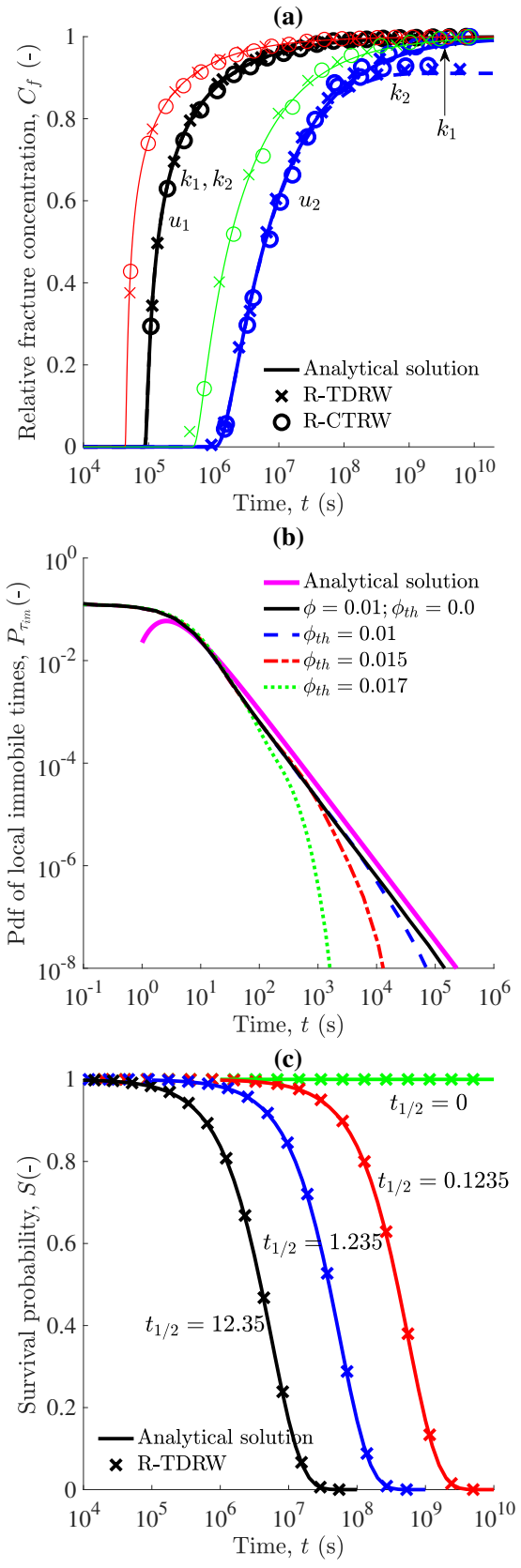

Figure 3: (a) Relative concentration in the fracture at position $L = 0.05$ m (red and green curves) and 0.1 m (black and blue curves) for the set of parameters *Param1* computed with solution (11) (lines), R-TDRW (crosses) and UR-TDRW (circles). (b) Immobile local time distribution computed from solution (A.10) (large solid magenta line) and R-TDRW for various porosity fields (from solid black to dotted green lines). (c) Survival probability computed with solution (12) (solid lines) and R-TDRW (crosses) for various values of $t_{1/2}$.

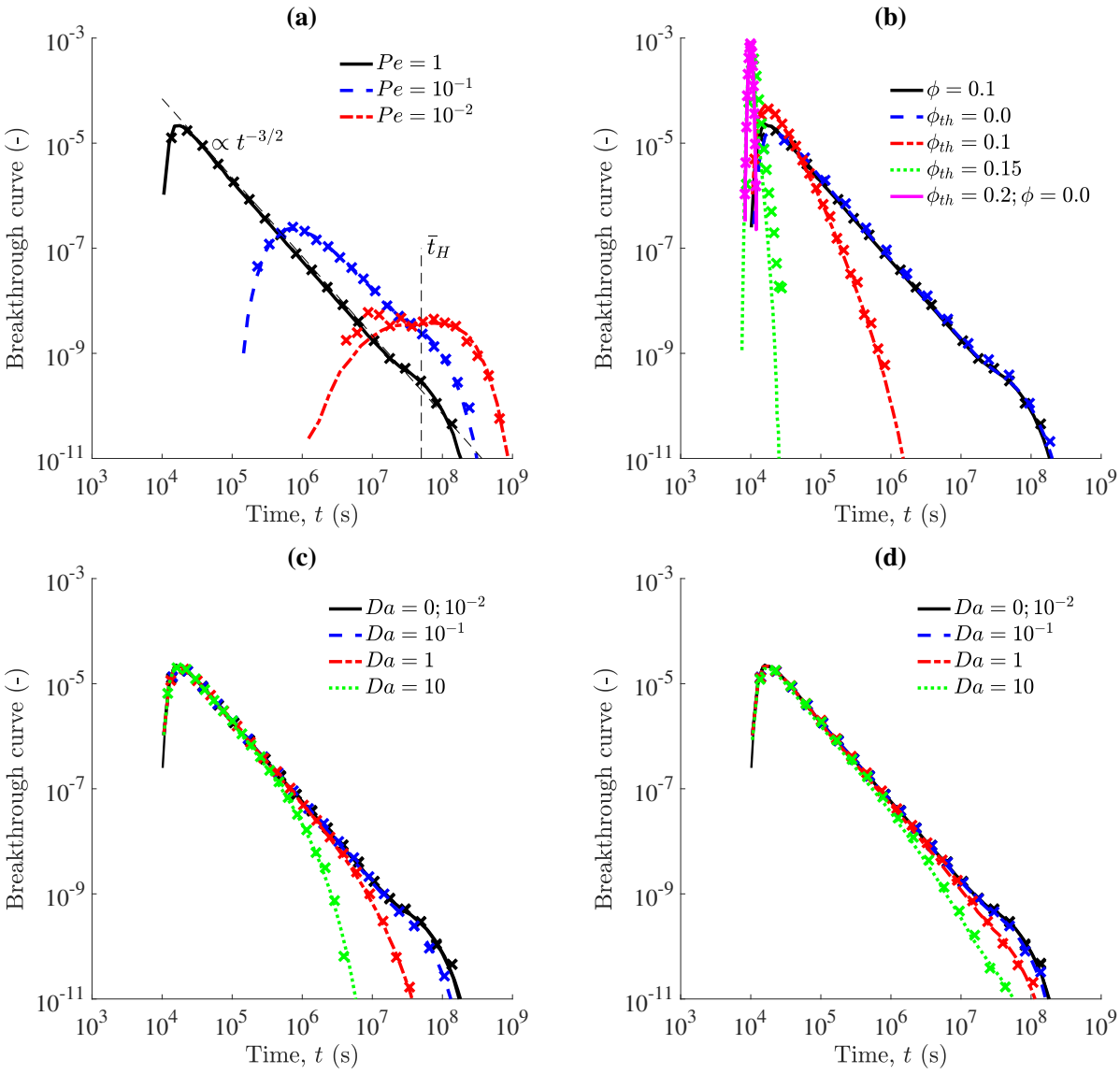

Figure 4: Breakthrough curves obtained with the R-TDRW (lines) and UR-TDRW (symbols) methods for various values of (a) Pe, (b) ϕ_{th} and (c,d) Da. (a,c,d all curves and b solid black line) Homogeneous and (b from dashed blue to dotted green lines) heterogeneous porosity fields are considered with (a,b) no reaction ($Da = 0$), (c) linear and (d) complex reactions.

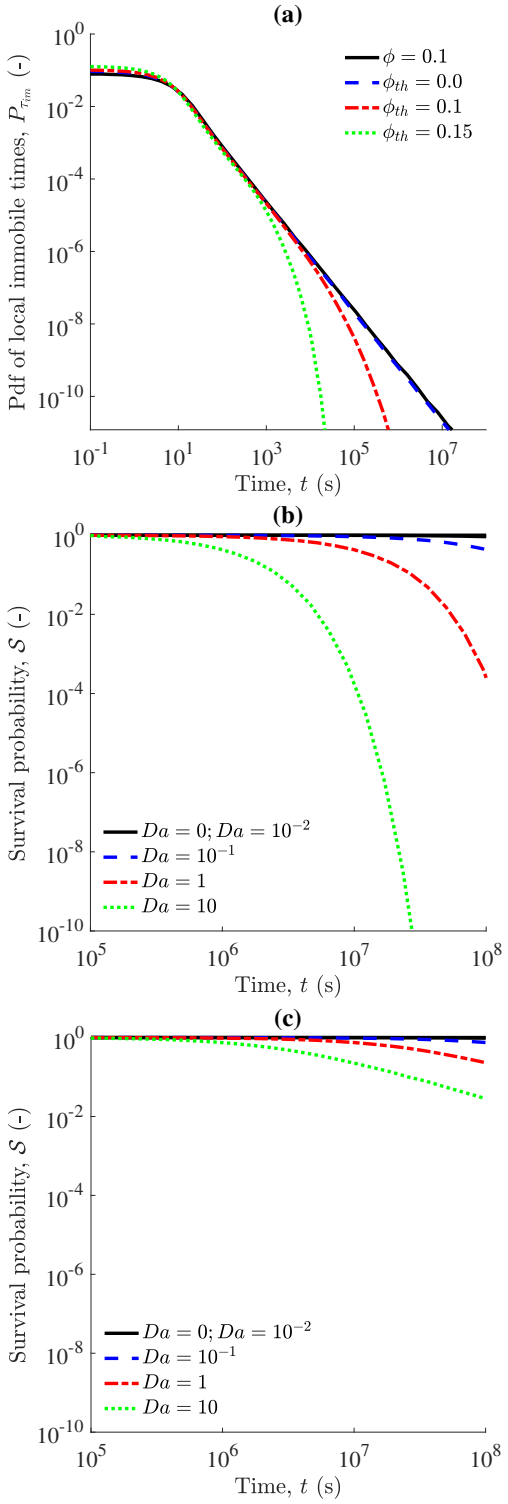

Figure 5: (a) Pdfs of local immobile times for homogeneous (solid black line) and heterogeneous (from dashed blue to dotted green lines) porosity fields and (b-c) survival probabilities for homogeneous matrix with (b) linear and (c) non-linear reaction for various values of Da. These results are computed with the R-TDRW method.